https://doi.org/10.1016/j.jsv.2021.116226

An Elastodynamic Reciprocity Theorem-based Closed-form Solution to Second Harmonic Generation of Lamb Waves by A Fatigue Crack: *Theory & Experimental Validation*

Lei Xu[a, §], Yiyin Su[a, §], Kai Wang[b], Xiongbin Yang[a], Shenfang Yuan[c] and Zhongqing Su[a, d, e*]

[a] Department of Mechanical Engineering
The Hong Kong Polytechnic University, Kowloon, Hong Kong SAR

[b] Department of Aeronautical and Aviation Engineering
The Hong Kong Polytechnic University, Kowloon, Hong Kong SAR

[c] State Key Lab of Mechanics and Control of Mechanical Structures
Nanjing University of Aeronautics and Astronautics, Nanjing 210016, P.R. China

[d] The Hong Kong Polytechnic University Shenzhen Research Institute
Shenzhen 518057, P.R. China

[e] School of Astronautics, Northwestern Polytechnical University, Xi'an, 710072, P.R. China

submitted to ***Journal of Sound and Vibration***

(initially submitted on 9th December 2020; revised and re-submitted on 25th March 2021 for R1; revised and re-submitted on 15th April 2021 for R2; revised and re-submitted on 9th May 2021)

[§] These authors contributed equally to this work.
[*] To whom correspondence should be addressed. Tel.: +852-2766-7818, Fax: +852-2365-4703;
Email: Zhongqing.Su@polyu.edu.hk (Prof. Zhongqing Su, *Ph.D*)

Abstract

Characterization of small-scale damage (with dimensions smaller than 1/10 of the probing wavelength) using nonlinear guided ultrasonic waves (GUWs) has been practiced over years, numerically and experimentally. To compensate for the insufficiency of analytical solutions that are able to interpret the underlying physical aspects of nonlinearity in GUWs induced by the small-scale damage and in particular fatigue damage, a new theoretical model based on the elastodynamic reciprocity theorem is developed. The model yields a closed-form solution to the modulation mechanism of a fatigue crack with 'breathing' attributes on Lamb wave propagation, gaining insight into the generation of second harmonics in Lamb waves. The model depicts the 'breathing' crack as an additional wave source imposing extra forces on crack surfaces that is equivalent to the integral of the stress tensor, and the source interferes with the wavefield of the original probing wave. In a time-frequency domain, this additional wave source is linked to the second harmonic generation in spectra. By virtue of the model, a nonlinear damage indicator, governed by the quantified second harmonic generated by the crack, is defined, to calibrate crack severity quantitatively. Finite element simulation is performed to verify the analytical model and demonstrate its accuracy when used for evaluating damage onset. Proof-of-concept experimental validation is conducted to verify the proportional trend of the damage indicator with respect to damage severity. This elastodynamic reciprocity-driven model and the closed-form solution shed light, from an analytical perspective, on the nonlinear interaction of GUWs with damage of small scale featuring 'breathing' attributes.

***Keywords*:** damage detection; contact acoustic nonlinearity; second harmonic generation; fatigue crack; elastodynamic reciprocity; Lamb wave

1. Introduction

The superior sensitivity of higher order harmonics embodied in guided ultrasonic waves (GUWs) to the microstructural evolution and material degradation has been broadly exploited, to develop high-precision nondestructive evaluation, condition monitoring, material state awareness and structural health monitoring techniques [1-8]. The higher order harmonics can be generated upon nonlinear interaction between a probing wave and microstructural degradation in a waveguide that is associated with dislocation, phase change, void nucleation and plastic deformation. There is a rich body of literature, in numerical or experimental natures [9-12], to reveal that the higher order harmonics of GUWs are more sensitive to contact-type defect (*e.g.*, fatigue cracks or delamination under the modulation of external loads), yet less affected by ambient variations (*e.g.*, environmental noise or temperature fluctuation) than the linear features of GUWs including the coefficients of wave transmission/reflection, distortion of waveform, and delay in wave arrival time [13-21]. Amongst the higher order harmonics, the second order harmonics are extensively explored, owing to their relatively stronger magnitudes and easier acquisition, compared with harmonics of higher orders.

Approaches making use of the second harmonics of GUWs and in particular those of Lamb waves, for the purposes of material characterization and damage evaluation, have primarily been developed based on the premise that the second harmonic generation can be attributed to two sources: i) the nonlinear material elasticity of the waveguide [22-24], and ii) the damage-induced contact acoustic nonlinearity (CAN) [25, 26]. For the former, the continuous material deterioration under cyclic loads (*e.g.*, dislocation dipoles, slip bands and micro-cracks) leads to deviation in intrinsic constitutive properties of the waveguide material, and the nonlinearity in constitutive properties consequently induces the second harmonic generation. This phenomenon can be rigorously interpreted by physics-based models. Representatively, the Hikata model, first established by Hikata *et al.* [27, 28] and further extended by Cash and Cai [29], links the contribution of screw and edge dislocations in the material to the magnitude of generated second harmonics. Chen and Qu [30] extended the Hikata model and proposed a solution to the pure and mixed dislocations in anisotropic crystals with orientation-dependent line energy, and the model was proven accurate in molecular dynamic simulation when it was used to evaluate variable dislocation lengths. Cantrell [31] investigated the effect of dislocation dipoles mutually trapped in wavy-slip on the generation of nonlinearity in GUWs propagating in various metals including crystalline nickel, aluminium alloys and copper single crystals, and revealed the correlation of acoustic nonlinearity with the density of dislocation dipoles and the dipole height. Based on that, Cantrell predicted the rise in the magnitude of the second harmonics by considering the interaction between precipitates and dislocations [32].

As far as the CAN concerned, the modulation of a contact-type defect, for instance a fatigue crack, on propagating GUWs is a key driving force to trigger the generation of nonlinear wave features. When a probing GUW traverses a contact-type crack or when the crack is modulated by an external excitation, the crack opens and closes, respectively during the tensile and compressive phases of the probing GUW, and such a crack is impersonated as the 'breathing' crack. Good supply of research has rigorously examined the scattering and second harmonic generation by a 'breathing' crack. Rose *et. al.* [33] represented the crack as a displacement discontinuity in the waveguide. The displacement discontinuity induces equivalent forces at the crack location, which generate additional wave to interfere in the original global wavefield. Achenbach *et. al.* [34, 35] investigated the scattering of elastic waves by a small-scale crack, and depicted the scattered waves from the crack as the radiated waves generated by an equivalent force, considering the sufficient small characteristic dimensions of the crack when compared with the wavelength of the incident wave. Shen and Giurgiutiu [36] simulated the nonlinear interaction between Lamb waves and a 'breathing' crack using a finite element (FE) method, and clarified a monotonic increase of the generated second harmonic against the crack severity. Yang *et al*. [6, 37] conducted numerical and experimental research on the second harmonic generation in low-frequency Lamb waves that was triggered by fatigue cracks, to conclude that the magnitude of the second harmonic induced by the interaction between the fundamental symmetric Lamb mode (S_0) and fatigue crack is much higher than that by the fundamental antisymmetric Lamb mode (A_0). Zhao *et al*. [38, 39] constructed a numerical model containing randomly distributed micro-cracks, to explore the second harmonic generation in low-frequency S_0 caused by these micro-cracks using a Monte Carlo simulation method. The simulation illuminated that the magnitude of the second harmonic is proportional to the crack density and propagation distance of Lamb waves in the cracking region, but is not correlated to the friction state of the micro-crack surfaces.

With that being said, most approaches exploring the second harmonic generation in GUWs are of a nature of either numerical simulation or experimental observation, and there is obvious lack of analytical interrogation to shed light on underlying physical aspects of nonlinearity in Lamb waves induced by small-scale damage and 'breathing' fatigue cracks in particular. Compared with the acoustic nonlinearity arising from the nonlinear elasticity of materials which can be thoroughly interpreted by physics-based models, rigorous theoretical derivation on the crack-induced second harmonic generation is still deficient. Among limited effort, Nazarov and Sutin [40] proposed a physical model to explain the phenomena observed in experiment and illustrated the high acoustic nonlinearity in the medium containing uniformly distributed and randomly oriented penny-shape micro-cracks. The model describes the crack behavior as an elastic contact of two rough surfaces, pressing one to the other under the action of internal stress in the surrounding solids. It has also been demonstrated that the presence of cracks results in strong variation in the quadratic and cubic nonlinearity parameters. The above model was later used to quantitatively determine the contribution of an evolving fatigue crack in a wavy slip metal to the acoustic nonlinearity in GUWs [41]. In the model, the distributed cracks were simplified as a single, holistic damage to alter the mechanical properties of the medium. However, when extended to scenarios in which a localized crack, rather than a multitude of distributed cracks, exists in the medium (*e.g.*, a corner crack near a fastener hole), the model becomes not tenable.

In recognition of the insufficiency of analytical solutions able to interpret the underlying physics of nonlinearity in GUWs induced by small-scale damage and in particular a fatigue crack with 'breathing' attributes, an analytical model is proposed in this study, based on the elastodynamic reciprocity theorem [33, 42-44]. The crack considered in the model is of a microscopic degree and under a stress-free state, namely in the absence of any external load. The model equates the 'breathing' crack as an additional wave source to impose extra forces equivalent to the integral of the stress on the crack surfaces, which interferes with the wavefield of the original probing Lamb wave. By performing a time-frequency analysis, this additional source is linked to the second harmonic generation in spectra. Residing on the elastodynamic reciprocity theorem, a closed-form solution to the magnitude of the 'breathing' crack-induced second harmonic is obtained. A nonlinear damage indicator is further defined by virtue of the closed-form solution, to calibrate the crack severity in a quantitative manner. FE simulation and experimental validation are respectively conducted to validate the model and examine its accuracy when used for evaluating embryonic fatigue cracks.

2. Elastodynamic Reciprocity-driven Model and Closed-form Solution

To analytically scrutinize the generation mechanism of second harmonic in a probing Lamb wave, upon the nonlinear interaction between the wave and a 'breathing' fatigue crack, an analytical model, based on the elastodynamic reciprocity theorem, is developed.

2.1 Lamb Waves Generated by A Time-harmonic Point Force

When a probing Lamb wave interacts with a 'breathing' crack, the wave can traverse through the crack without being distorted during the compressive phase of the wave; in the contrast, the wave is intercepted by the crack during the tensile phase of the wave [45-47]. To depict such two alternate periods in a wave cycle, a *second excitation force* is introduced in the analytical model, to supplant the stress generated on the crack surfaces during this interaction. To facilitate this, the probing Lamb wave generated by a time-harmonic point force is defined first.

Comprising symmetric and antisymmetric modes, a Lamb wave in a thin plate-like waveguide in a stress-free state, can be excited using a time-harmonic vertical point force P and a horizontal point force Q applied simultaneously, see **Fig. 1**, as [48, 49]

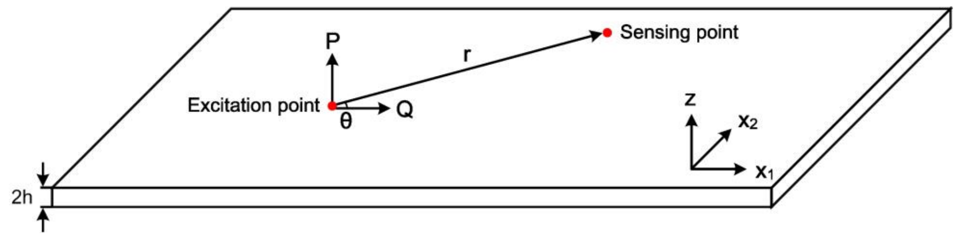

Figure 1. Schematic of Lamb wave generation by a point force.

$$u_\alpha^n = \frac{1}{k_n^\omega} V^n(z) \frac{\partial \varphi(x_1, x_2)}{\partial x_\alpha} e^{i\omega t}, \tag{1}$$

$$u_z^n = W^n(z) \varphi(x_1, x_2) e^{i\omega t}. \tag{2}$$

In the above, u_α^n (α =0 or 1) and u_z^n denote the in-plane displacement (within the x_1x_2 -plane) and out-of-plane displacement of the n^{th} -order Lamb wave mode, respectively. ω and t are the angular frequency of the time-harmonic point force and the time, respectively. i is the imaginary unit. k_n^ω is the wavenumber of the n^{th} -order Lamb wave mode at ω. $\varphi(x_1, x_2)$ signifies the solution of the membrane equation in the x_1x_2 -plane, which satisfies

$$\nabla^2 \varphi(x_1, x_2) + (k_n^\omega)^2 \varphi(x_1, x_2) = 0. \tag{3}$$

$V^n(z)$ and $W^n(z)$ represent the in-plane and out-of-plane displacement functions of the n^{th}-order Lamb wave mode, respectively, which can be separated into the symmetric ($V_S^n(z)$ and $W_S^n(z)$) and antisymmetric ($V_A^n(z)$ and $W_A^n(z)$) modes, as

for symmetric modes

$$V_S^n(z) = s_1\cos(pz) + s_2\cos(qz), \tag{4}$$

$$W_S^n(z) = s_3\sin(pz) + s_4\sin(qz), \tag{5}$$

for antisymmetric modes

$$V_A^n(z) = a_1\sin(pz) + a_2\sin(qz), \tag{6}$$

$$W_A^n(z) = a_3\cos(pz) + a_4\cos(qz), \tag{7}$$

where

$$p^2 = \frac{\omega^2}{c_L^2} - (k_n^\omega)^2, \quad c_L^2 = \frac{2\mu(1-\upsilon)}{\rho(1-\upsilon)}, \tag{8a}$$

$$q^2 = \frac{\omega^2}{c_T^2} - (k_n^\omega)^2, \quad c_T^2 = \frac{\mu}{\rho}. \tag{8b}$$

s_1, s_2, s_3, s_4 and a_1, a_2, a_3, a_4 are two series of coefficients, depending on p, q, and k_n^ω. c_L and c_T are the velocities of the longitudinal and transverse wave modes, respectively, which jointly constitute the Lamb wave. μ is the shear modulus of the plate, υ the Poisson's ratio, and ρ the density.

In a cylindrical coordinate system, the wavefield of the outgoing symmetric Lamb wave modes (using symmetric modes as an example – the mode to be explored in the analytical model) generated by the time-harmonic point force can be written as

$$u_r^n = V_S^n(z)\phi'(k_n^\omega r)\cos\theta, \tag{9}$$

$$u_\theta^n = (-\frac{1}{k_n^\omega r})V_S^n(z)\phi(k_n^\omega r)\sin\theta, \tag{10}$$

$$u_z^n = W_S^n(z)\phi(k_n^\omega r)\cos\theta, \tag{11}$$

where u_r^n, u_θ^n and u_z^n are the radial, circumferential and out-of-plane displacement components of the n^{th}-order Lamb wave mode, respectively. r and θ are coordinates of the sensing point, at which the propagating wave signal is captured. ϕ and ϕ' are the first-order Hankel function of the second kind and its derivative, respectively. The stress component along the radial direction induced by the probing wave for the n^{th}-order Lamb wave mode, σ_{rr}^n, can be expressed as [48]

$$\sigma_{rr}^n = \sum\nolimits_{rr}^{S_n}(z)\phi(k_n^\omega r)\cos\theta - \overline{\sum\nolimits_{rr}^{S_n}(z)}\,[\frac{1}{r}\phi'(k_n^\omega r) - \frac{1}{k_n^\omega r^2}]\cos\theta. \tag{12}$$

$\sum\nolimits_{rr}^{S_n}(z)$ and $\overline{\sum\nolimits_{rr}^{S_n}(z)}$ are two functions of μ, p, q and waveguide thickness ($2h$).

Recalling the elastodynamic reciprocity theorem relating two elastodynamic states of the same body V and surface S, which can be expressed as

$$\int_V (f_i^A u_i^B - f_i^B u_j^A)dV = \int_S (u_i^A \sigma_{ij}^B - u_i^B \sigma_{ij}^A)n_j dS, \tag{13}$$

where A and B represent two elastodynamic states, $f_i^A(f_i^B)$, $u_i^A(u_i^B)$ and $\sigma_{ij}^A(\sigma_{ij}^B)$ are body force, displacement and stress, respectively. n_j is the component of outward normal to S. The amplitudes of the symmetric Lamb wave modes of different orders, generated by a time-harmonic point force, can be determined explicitly at a given circular frequency. Based on the recursive relation of the Hankel function, the Lamb wave modes can be obtained as a function of the time-harmonic vertical point force P and horizontal point force Q, wave propagation distance and direction [48], as follows,

$$u_r^{PS} = f_v^r(P,r) = -\sum_{n=0}^{m} C_n^{S,\omega} V_S^n(z) H_1^{(2)}(k_n^\omega r)P, \tag{14a}$$

$$u_z^{PS} = f_v^z(P,r) = \sum_{n=0}^{m} C_n^{S,\omega} W_S^n(z) H_0^{(2)}(k_n^\omega r)P, \tag{14b}$$

$$u_r^{QS} = f_h^r(Q,r,\theta) = \sum_{n=0}^{m} A_n^{S,\omega} V_S^n(z)[H_0^{(2)}(k_n^{\omega} r) - \frac{1}{k_n r} H_1^{(2)}(k_n^{\omega} r)]Q\cos\theta, \tag{15a}$$

$$u_z^{QS} = f_h^z(Q,r,\theta) = \sum_{n=0}^{m} A_n^{S,\omega} W_S^n(z) H_1^{(2)}(k_n^{\omega} r) Q\cos\theta. \tag{15b}$$

Here, f_v^r (or f_h^r) and f_v^z (or f_h^z) are the magnitude functions of the in-plane and out-of-plane displacement of the symmetric Lamb wave modes, generated by a vertical (or horizontal) point force – namely P (or Q). m is the number of Lamb wave modes generated in the waveguide. Superscripts PS and QS indicate the symmetric modes generated by vertical force P and horizontal force Q, respectively. $H_p^{(2)}(\cdot)$ denotes the p^{th}-order Hankel function of the second kind (p = 0 or 1). $C_n^{S,\omega}$ and $A_n^{S,\omega}$ are the magnitude coefficients which can be expressed as a function of the applied point force and the modal energy flux as follows

$$C_n^{S,\omega} = \frac{k_n^{\omega}}{4i} \frac{W_S^n(z)}{I_{nn}^S}, \tag{16a}$$

$$A_n^{S,\omega} = \frac{k_n^{\omega}}{4i} \frac{V_S^n(z)}{I_{nn}^S}. \tag{16b}$$

In the above, I_{nn}^S is the energy carried by the n^{th}-order symmetric Lamb wave mode which can be expressed as

$$I_{nn}^S = \mu[c_1 cos^2(ph) + c_2 cos^2(qh)], \tag{17}$$

where

$$c_1 = \frac{(k_n^2 - q^2)(k_n^2 + q^2)}{2q^3 k_n^3}[2qh(k_n^2 - q^2) - (k_n^2 + 7q^2) sin(2qh)]$$
$$c_2 = \frac{k_n^2 + q^2}{p k_n^3}[4k_n^2 ph + 2(k_n^2 - 2p^2) sin(2ph)].$$

Validity of the above theoretical derivation is to be verified in Section 4.1.

2.2 'Breathing' Crack-induced Second Harmonic

Consider a 3-D, thin plate-like waveguide under a stress-free state, on the upper surface of which there exists a non-penetrating (occupying partial thickness of the waveguide), small-scale fatigue crack (with length and depth of the crack being smaller than 1/10 of the wavelength of the probing Lamb wave) with ‘breathing’ attributes. The crack locates between the excitation point and a sensing point from which Lamb waves, upon interaction with the crack, are captured. The center of the crack is r_1 from the excitation point, and r_2 from the sensing point, as schematically illustrated in **Fig. 2**.

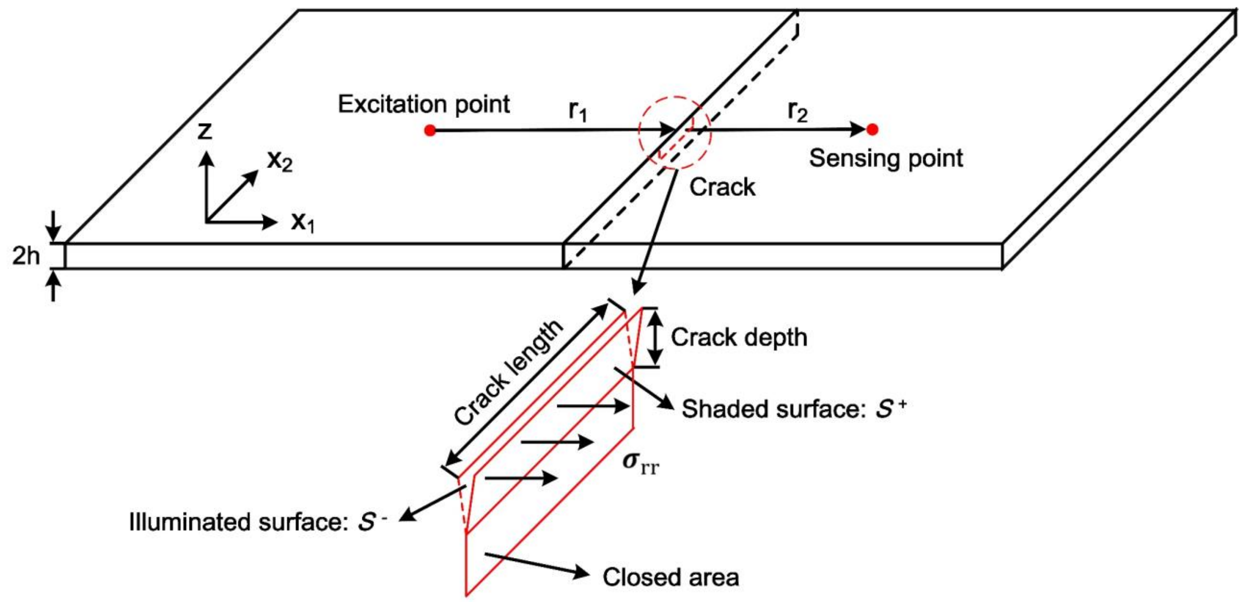

Figure 2. Schematic of Lamb wave excitation and acquisition in a plate waveguide containing a ‘breathing’ crack.

During the tensile phase of wave propagation, the two crack surfaces are apart one from the other, partially or entirely. The crack surfaces are deemed smooth due to the fairly small dimensions of the crack, as a consequence of which the effect of vertical force at the crack on the second harmonic generation is not considered. Let S stand for the opening area of the crack surface, which can further be divided as S^+ and S^-, referred to as the *shaded* and *illuminated* surfaces, respectively, in **Fig. 2**. As a result of the traction-free state on S^+ and S^-, the normal stress in x_1 direction on S^+ satisfies the following criterion during wave propagation:

$$\sigma(x,t) \geq 0. \quad x \in S^+ \tag{18}$$

The probing wave can propagate through the crack without distortion during the compressive phase in a wave cycle, while the wave is intercepted by the crack during tensile phase. Allowing for the small scale of the crack (with dimensions smaller than 1/10 of the probing wavelength), a pair of time-harmonic, concentrated, horizontal point forces, F^+ and F^-, is introduced to supplant the effect of the stress on S^+ and S^-, respectively, to investigate the crack-induced second harmonic. F^+ and F^- are equal in amplitude but opposite in direction. Taking F^+ as an example, the amplitude of F^+ equals to the difference between (i) the integral value of the normal stress in x_1 direction on S^+ when the waveguide is intact, and (ii) the integral value of the normal stress in x_1 direction on S^+ when the waveguide is cracked, as

$$F^+ = \int_{S^+} |\sigma_{rr}^n(x,t)|_{intact}\, ds - \int_{S^+} |\sigma_{rr}^n(x,t)|_{cracked}\, ds = \begin{cases} 0, & during\ compressive\ phase \\ \int_{S^+} |\sigma_{rr}^n(x,t)|_{intact}\, ds, & during\ tensile\ phase. \end{cases} \tag{19}$$

The identical manipulation is also applied to F^- on S^-. In the above, $|\sigma_{rr}^n(x,t)|_{cracked}$ represents the absolute value of the normal stress component on crack surface in the cracked waveguide, and $|\sigma_{rr}^n(x,t)|_{intact}$ signifies the absolute value of the normal stress component on the same surface in an intact waveguide. The pair of F^+ and F^- serves as an equivalent second excitation on the crack surface, to interfere with the original wavefield in the waveguide, and therefore it is referred to as *the second excitation force* hereinafter. Considering the second excitation force is defined based on the stress component under intact scenario, all other stress components on the two crack surfaces, as well as the sliding effect of the crack, are ignored here, as the normal stress in x_1

direction dominates the stress field in the intact waveguide, and is higher than other stress components by several orders of magnitude [48].

The stress component along the radial direction induced by the probing wave, as analytically obtained in Section 2.1 (i.e., Eq. (12)), is substituted into Eq. (19). With Eq. (19), the amplitude of the second excitation force on the crack surface, in pace with the cyclic probing wave, is obtained analytically and shown in **Fig. 3(a)**. The second excitation force exists in the tensile phase of the probing Lamb wave propagation only, and otherwise vanishes. The force is then scrutinized in the frequency domain, in which it is decomposed into two equivalent forces, respectively at fundamental frequency (ω) and at the double excitation frequency (2ω): i) the first equivalent force, ${F_{eq1}}^{+}$, which is a sinusoidal signal at ω, **Fig. 3(b)**; and ii) the second equivalent force, ${F_{eq2}}^{+}$, which is the absolute value of ${F_{eq1}}^{+}$ at 2ω, as shown in **Fig. 3(c)**. Both the magnitudes of ${F_{eq1}}^{+}$ and ${F_{eq2}}^{+}$ are the half of that of F^{+}. Such decomposition warrants that the summation of ${F_{eq1}}^{+}$ and ${F_{eq2}}^{+}$ equates F^{+}. Applied with the continuous-time Fourier transform (FT), it can be observed in **Fig. 4** that ${F_{eq1}}^{+}$ corresponds to a wave component at the fundamental frequency (ω) and $F_{eq2}{}^{+}$ to a wave component at 2ω – the source to generate the second harmonic.

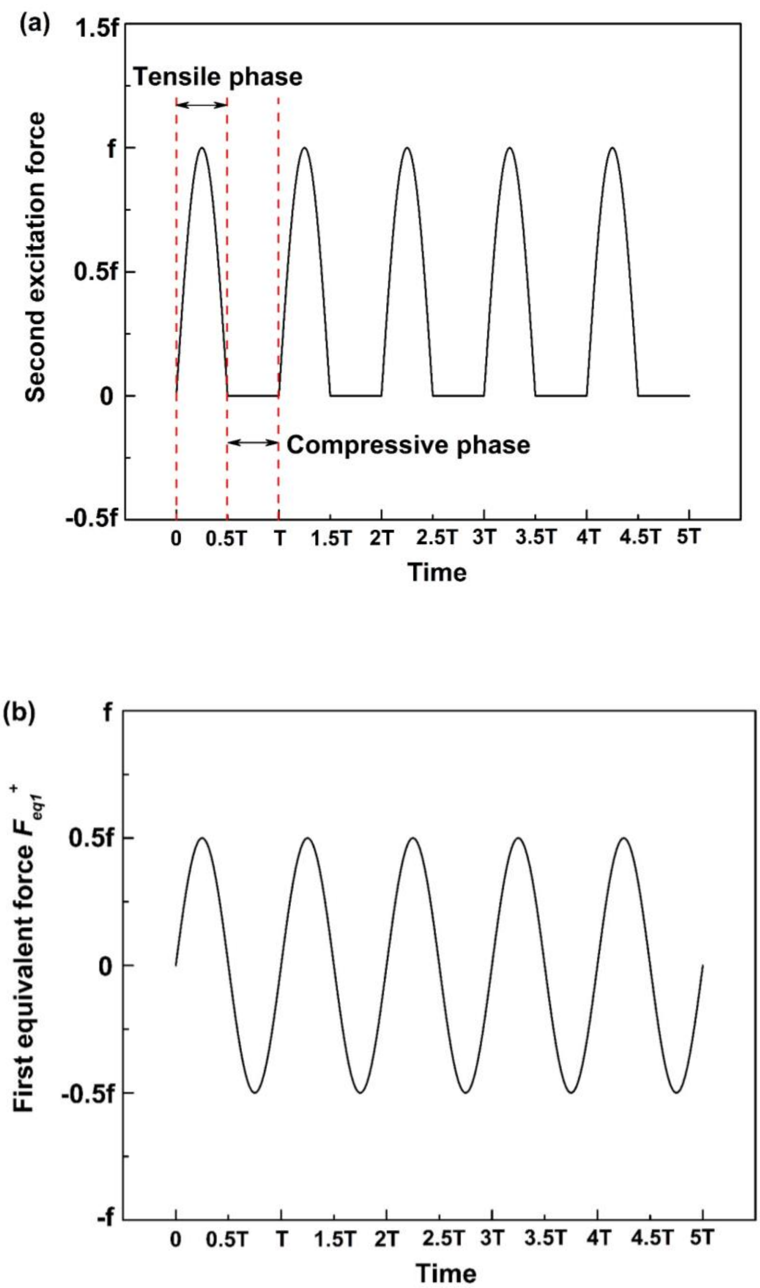

Figure 3. (a) The second excitation force (F(t)) generated by the 'breathing' crack, (b) F_{eq1} and (c) F_{eq2} (f: the second excitation force (F(t)) calculated when the crack opens entirely during the tensile phase; T: the period of a wave cycle).

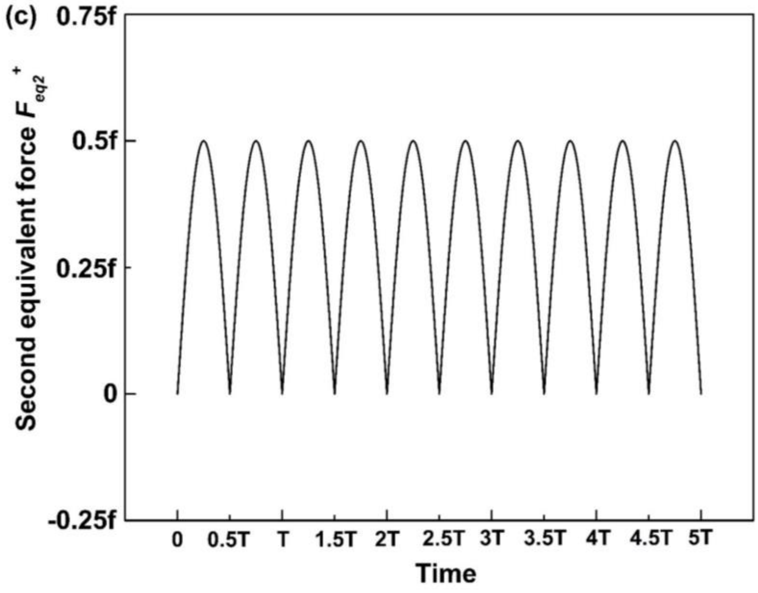

Figure 3. *Cont.*

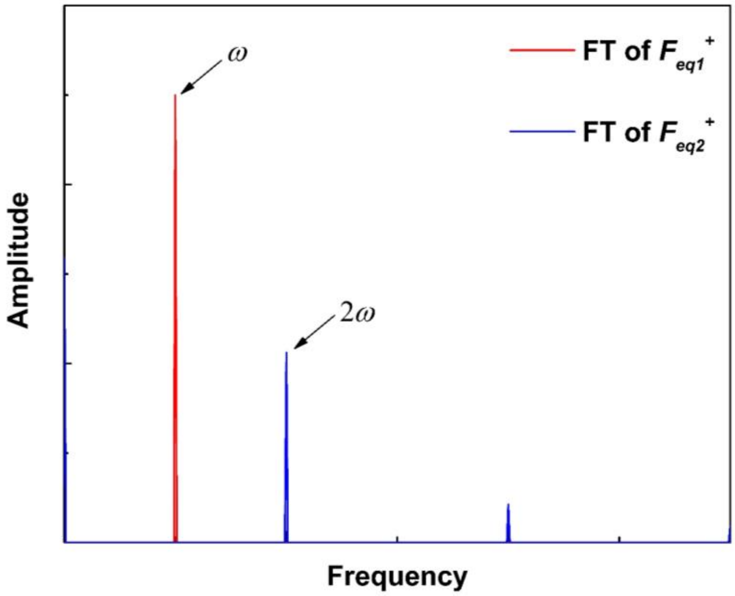

Figure 4. Spectra of F_{eq1} and F_{eq2} (ω: the fundamental frequency; 2ω: the double excitation frequency).

Knowing the source of the second harmonic generation, the amplitude of the second harmonic induced by the crack with 'breathing' attributes can be quantified explicitly and analytically. According to the magnitude functions of Lamb wave generated by a time-harmonic horizontal point force as described in Eqs. (15a) and (15b), the magnitude (u_r^{sh} and u_z^{sh}) of the second harmonic induced by $F_{eq2}{}^{+}$ and $F_{eq2}{}^{-}$ can be determined, in the cylindrical coordinate system, as

$$u_r^{sh} = f_h^r(2F_{eq2}{}^{+}, r_2, \theta) = \sum_{n=0}^{\infty} A_n^{S,2\omega} V_S^n(z)[H_0^{(2)}(k_n^{2\omega} r_2) - \frac{1}{k_n r_2} H_1^{(2)}(k_n^{2\omega} r_2)]\left|F_{eq2}{}^{+}\right|\cos\theta, \quad (20a)$$

$$u_z^{sh} = f_h^z(2F_{eq2}{}^{+}, r_2, \theta) = \sum_{n=0}^{\infty} A_n^{S,2\omega} W_S^n(z) H_1^{(2)}(k_n^{2\omega} r_2)\left|F_{eq2}{}^{+}\right|\cos\theta, \quad (20b)$$

where

$$A_n^{S,2\omega} = \frac{k_n^{2\omega}}{2i}\frac{V_S^n(z)}{I_{nn}^S}. \quad (21)$$

In the above, $k_n^{2\omega}$ signifies the wavenumber of n^{th}-order Lamb wave mode at 2ω, and $\left|F_{eq2}{}^{+}\right|$ the magnitude of $F_{eq2}{}^{+}$. Validity of the above theoretical derivation is to be verified in Section 4.2.

3. Nonlinear Damage Indicator

Equation (20) – a closed-form solution to the magnitude of the second harmonic generated by a ‘breathing’ crack, analytically depicts the CAN induced by the crack in Lamb waves. It offers possibility to inversely characterize a fatigue crack by virtue of the quantified second harmonic extracted from a captured Lamb wave signal. With such a philosophy, a nonlinear damage indicator is developed, for calibrating the severity of a fatigue crack quantitatively. The nonlinear damage indicator, β, is defined as the ratio of the magnitude of the generated second harmonic to that of the fundamental wave of the probing Lamb wave. Using the in-plane displacement of the fundamental symmetric mode (S_0) under the in-plane excitation as an example, β reads

$$\beta = \frac{|u_r^{sh,0}|}{|u_r^0|} \quad (22)$$

where $|u_r^0|$ and $|u_{\mathrm{r}}^{sh,0}|$ are the magnitudes of the in-plane displacement of the fundamental S_0 mode and the ‘breathing’ crack-triggered S_0 mode second harmonic, respectively, which can be calculated based on Eqs. (15a) and (20a).

Allowing for the micro-dimensions of an embryonic fatigue crack under investigation, the normal stress at the crack surface (S^+ and S^-) is constant across the entire crack surface (including the opening area and the closed area, see **Fig. 2**), and consequently the second excitation force introduced by the crack, as defined by Eq. (19), can be simplified as

$$F(t) = S_{Opening\ area} \cdot \sigma_{rr}^{n}(t), \tag{23}$$

where $S_{Opening\ area}$ is the opening surface area of the crack. In addition, the normal stress is primarily constant along the entire thickness of the waveguide (including the cracked and uncracked parts), provided the crack is not in the vicinity of the excitation point. To put it into perspective and by way of illustration, the normal stress in a 5-mm thick plate along x_1 direction that is generated by a time-harmonic point force with a magnitude of 1 *N*, is calculated using Eq. (12), in **Fig. 5**. It is noted in the figure that the normal stress, respectively measured at different locations (50, 100, 150 and 200 mm away from the excitation point), remains largely constant along the entire waveguide thickness when the crack is not in the vicinity of the excitation point.

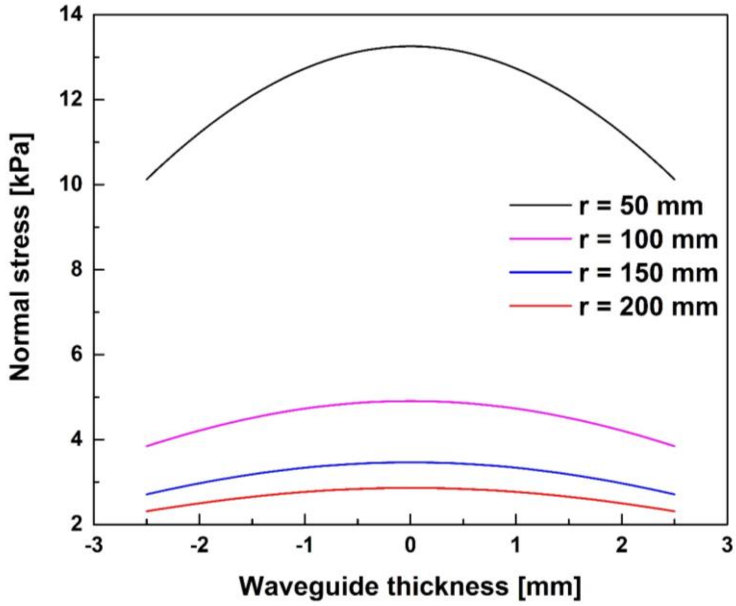

Figure 5. Normal stress along x_1 direction through waveguide thickness, measured at locations of different distances from the excitation point.

With a quasi-constant distribution of normal stress across the waveguide thickness, $F_{eq2}{}^{+}$, – the source to generate the second harmonic, is proven proportional to the surface area of the crack. Therefore, the magnitude of the second harmonic generated by the crack, as well as the damage indicator β, are also proportional to the area of the whole crack surface (including the opening area and the closed area). Such a conclusion is conducive to continuous monitoring and quantitative evaluation of a fatigue crack during its growth (to be detailed in simulation (Section 4) and experiment (Section 5)).

In conclusion, an elastodynamic reciprocity-driven model is proposed, on which basis the wavefields of a probing Lamb wave that is generated by a time-harmonic point force in both intact waveguide and the waveguide with a crack with 'breathing' attributes are respectively obtained, in an explicit and analytical manner. A closed-form solution to the magnitude of the generated second harmonic is established. With the magnitude of the generated second harmonic, a nonlinear damage indicator is defined, which is proven proportional to the crack surface area, to be used for quantitative evaluation of a fatigue crack in sequent sections.

4. Validation Using Three-dimensional Finite Element (FE) Simulation

The above analytical model and the closed-form solution are first validated using FE simulation. The magnitudes of both fundamental wave and crack-induced second harmonic, as well as the defined damage indicator, are calculated based on the magnitude functions of Lamb waves generated by a time-harmonic point force. In this section, the magnitude of the Lamb waves generated by a point force in an intact waveguide is first validated, followed by the verification of the magnitude of crack-induced second harmonic.

4.1 Validation of Lamb Waves Generated by A Time-harmonic Point Force

To validate Eqs. (14) and (15) derived based on the elastodynamic reciprocity theorem, a three-dimensional (3-D), plate-like waveguide (Young's modulus: 73 GPa; Poisson's ratio: 0.33; density: 2700 kg/m^3) is considered and modeled in ABAQUS®/EXPLICT. The waveguide measures 600 mm long, 500 mm wide and 5 mm thick. A 5-cycle Hanning-windowed sinusoidal toneburst at a central frequency of 180 kHz is excited, by simultaneously applying a pair of point forces with the magnitude of 1 N on the upper and lower surfaces of the waveguide, as a result of which only the symmetric Lamb wave modes are exited in the waveguide. Lamb wave signals are captured 50 mm from the excitation point, at up to six sensing points along the waveguide thickness (as illustrated in **Fig. 6**). These sensing points, labeled as SP1 – SP6, are scattered evenly with an interval of 0.5 mm between the upper and middle planes of the waveguide.

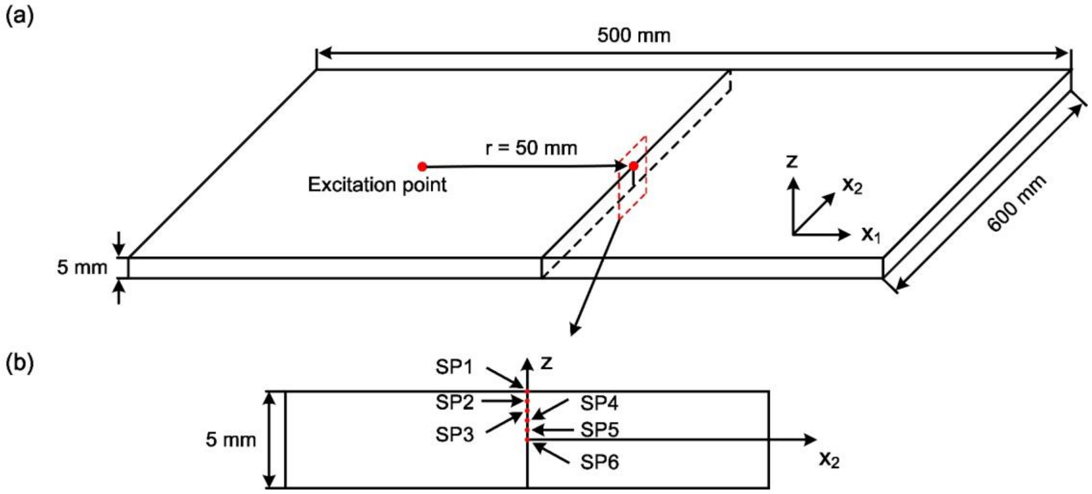

Figure 6. (a) Schematic of the 3-D FE model, and (b) locations of sensing points (right side-view).

An in-plane horizontal point force excitation (corresponding to Q in the analytical model) and an out-of-plane vertical excitation (P in the model) are respectively applied in FE. The radial component of the in-plane displacement along x_1 direction and the out-of-plane displacement along z direction at each sensing point are numerically captured, both of which constitute the symmetric Lamb wave mode. The in-plane and out-of-plane wave signals captured at SP1 – SP6 under the in-plane excitation scenario are presented in **Fig. 7**, and it can be observed that amplitudes of the radial displacement at different locations along waveguide depth remains largely unchanged; while amplitudes of the out-of-plane displacement changes remarkably, decreasing to zero at the middle plane of the waveguide, which is in agreement with the stress distribution of a symmetric Lamb wave mode. The second pulses in the wave signals are the boundary reflection.

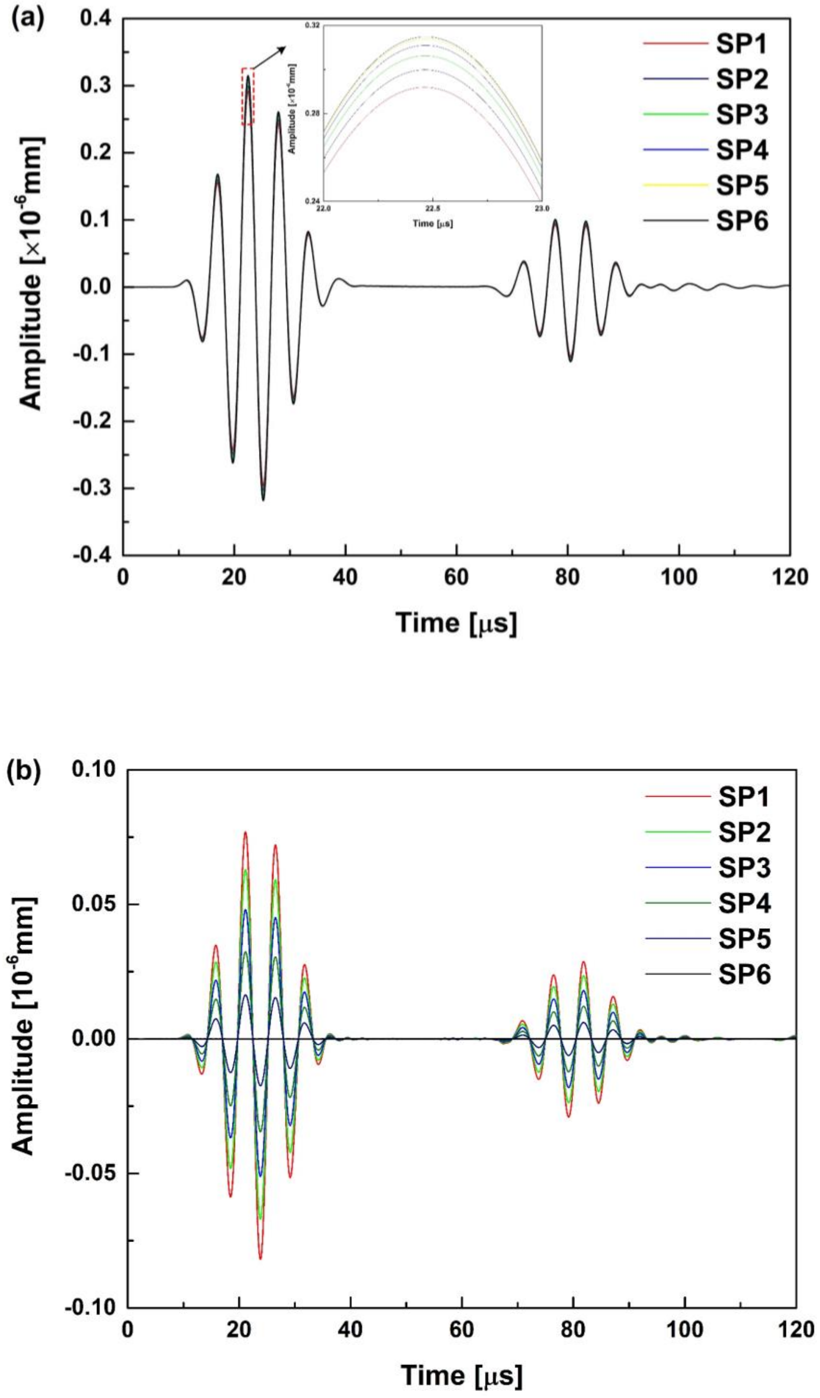

Figure 7. (a) In-plane, and (b) out-of-plane displacement captured at SP1– SP6, obtained from FE simulation under an in-plane excitation.

To evaluate the Lamb wave mode generated by the in-plane point force, the time-frequency analysis is performed, to obtain the spectra of the in-plane displacement of sensing points which are 50, 100, 150 and 200 mm away from the excitation point, as shown in **Figs. 8(a-d)**. Comparing the spectra with the dispersion curve of Lamb waves, it can be clearly observed that only S_0 mode is generated in the waveguide by the applied point force.

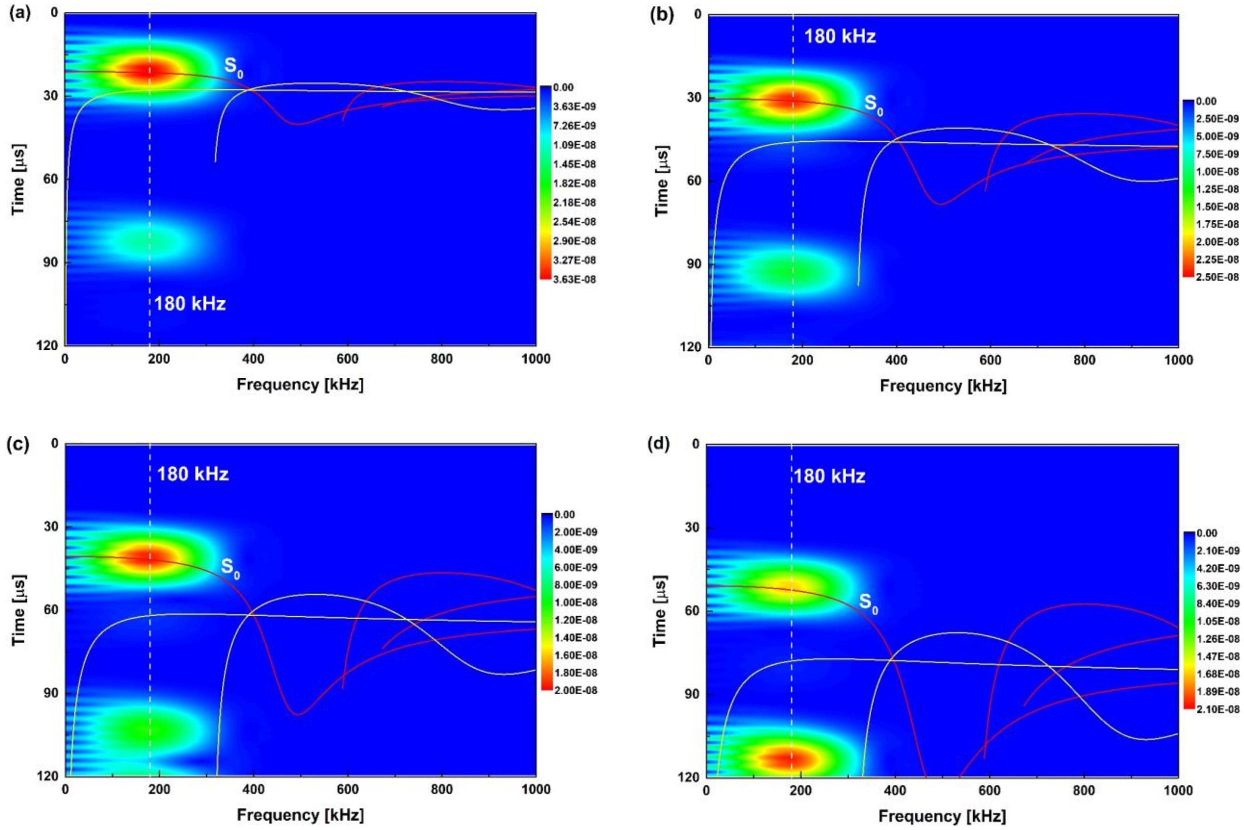

Figure 8. Spectra of the in-plane displacement of the sensing points which are (a) 50, (b) 100, (c) 150, and (d) 200 mm away from the excitation point.

Further, the magnitudes of symmetric Lamb wave modes at different depths of the waveguide, numerically obtained using FE and analytically derived using the theoretical model, are compared in **Fig. 9**. In **Fig. 9**, wave signals respectively captured 100, 150 and 200 mm away from the excitation point are also included for comparison.

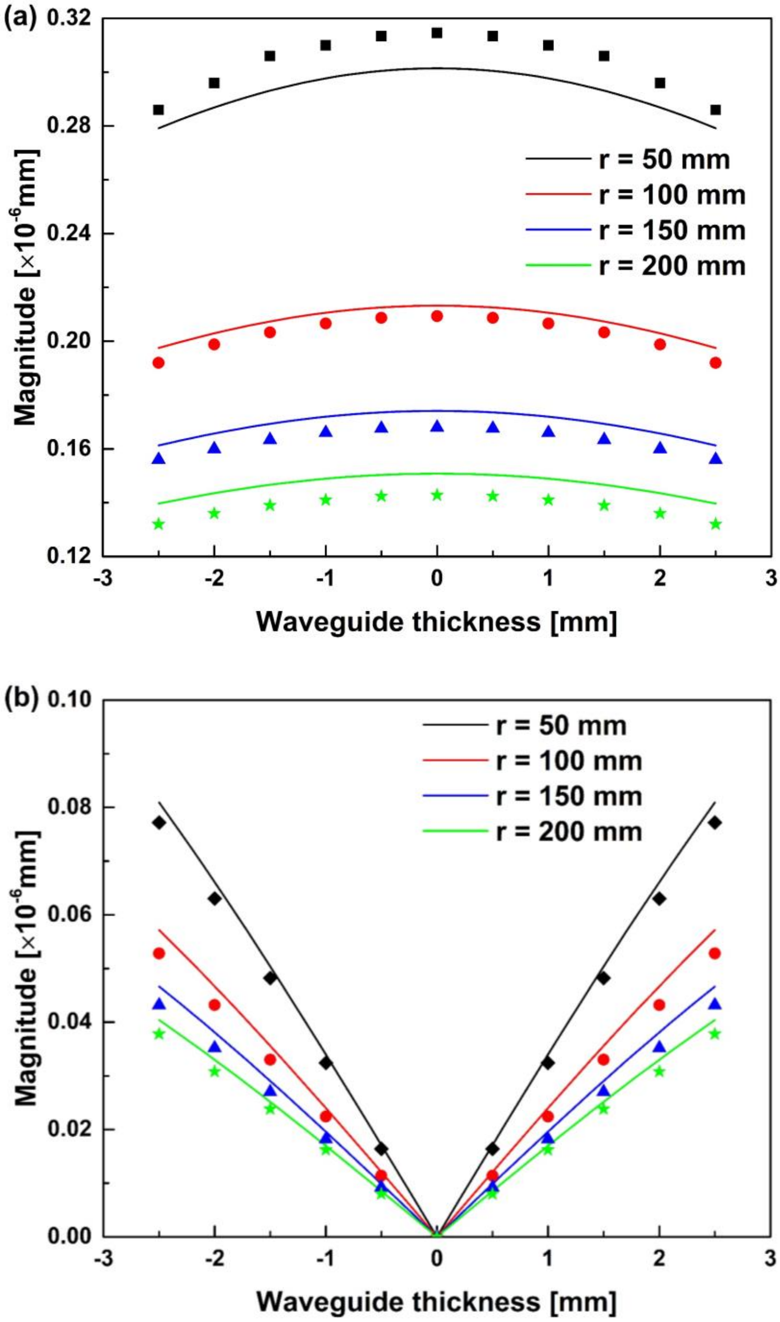

Figure 9. Comparison between the elastodynamic reciprocity-based analytical results and FE simulation: (a) in-plane, and (b) out-of-plane displacement magnitudes captured at different sensing points under an in-plane excitation. (solid: analytical results dots: numerical results)

Analogously, **Fig. 10** and **Fig. 11** compare the results obtained when an out-of-plane excitation is applied.

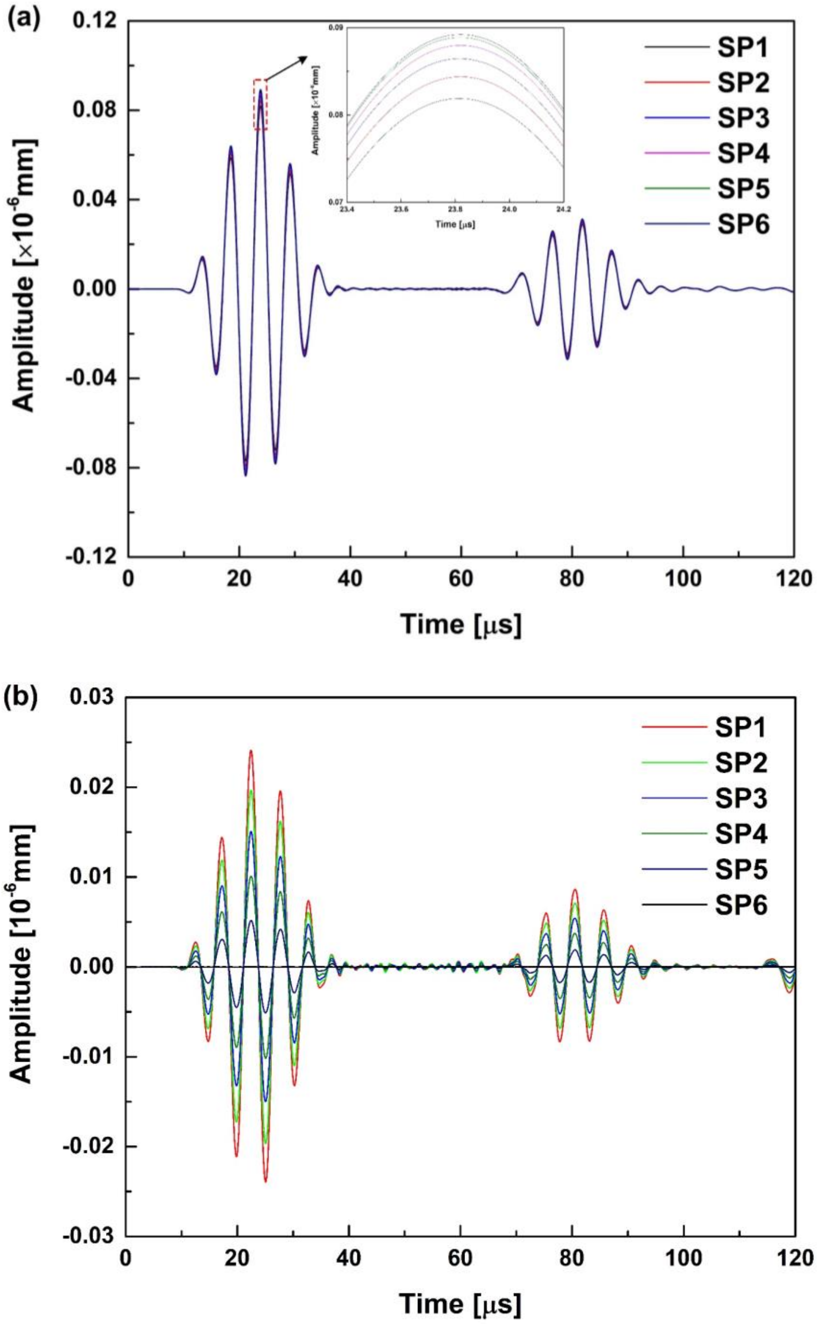

Figure 10. (a) In-plane, and (b) out-of-plane displacement captured at SP1– SP6, obtained from FE simulation under an out-of-plane excitation.

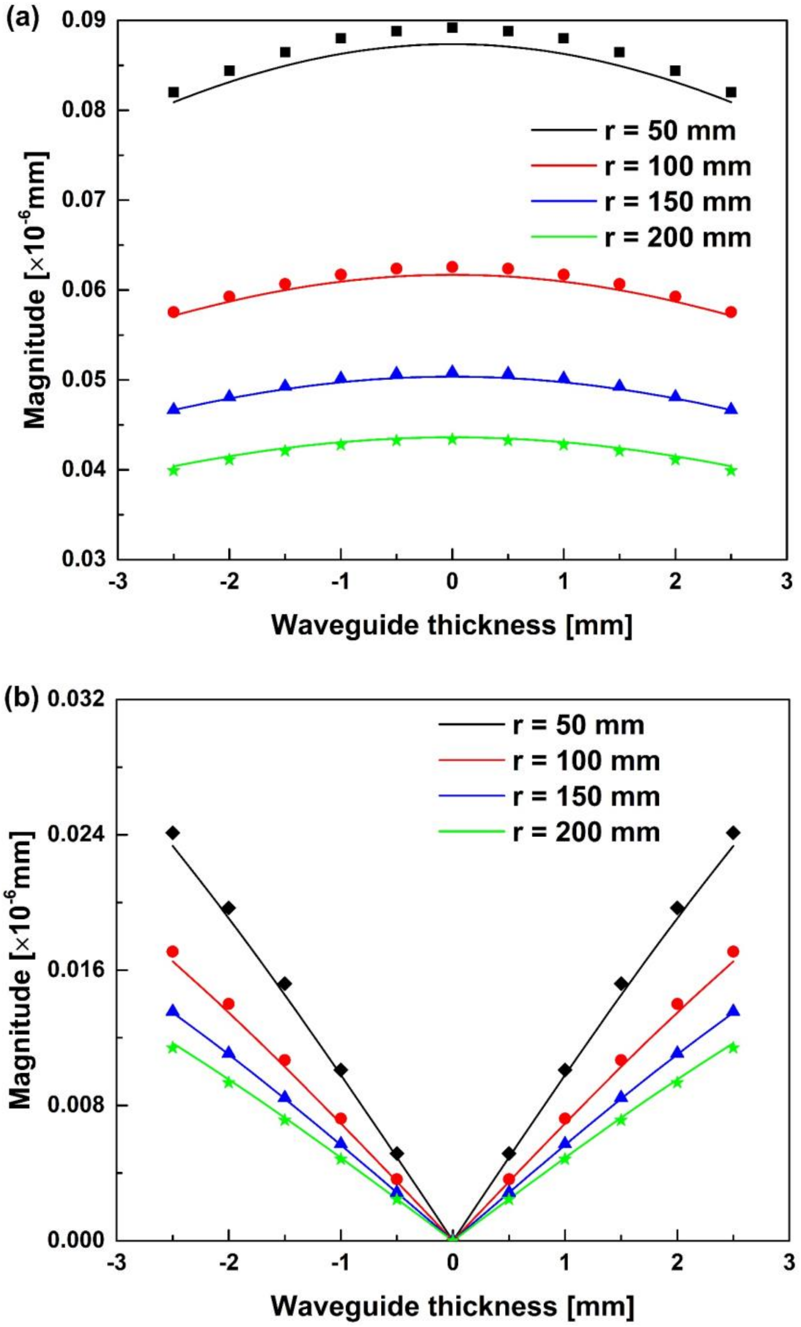

Figure 11. Comparison between the elastodynamic reciprocity-based analytical results and FE simulation: (a) in-plane, and (b) out-of-plane displacement magnitudes captured at different sensing points under an out-of-plane excitation. (solid: analytical results; dots: numerical results)

It is apparent that the numerical results are in good coincidence with the analytical results for both the in-plane (Eq. 14(a) and Eq.15(a)) and the out-of-plane (Eq.14(b) and Eq. 15(b)) scenarios, under either an in-plane or an out-of-plane excitation. This has validated the analytical model developed in Section 2.1.

4.2 Validation of 'Breathing' Crack-induced Second Harmonic

To validate the closed-form solution defined by Eq. (20), a surface-breaking, non-penetrating seam crack is modeled at the center of the above waveguide with the crack surface lying in x_2z-plane, see **Fig. 2**. The length of the crack is set to be 1 mm yet with different depths. To introduce the nonlinear 'breathing' behavior, the contact-pair interaction-based boundary condition is applied on the two crack surfaces [10], which permits separation of two surfaces but prohibits the penetration of FE nodes on each surface to the other. The seam crack with nonlinear 'breathing' behavior well reflects the dynamic attributes of a true fatigue crack in reality. As a consequence, the CAN due to the presence of a 'breathing' crack is introduced into the FE model. A sensing point, positioned 200 mm from the excitation point, captures the propagating Lamb waves in the waveguide in a 'pitch-catch' configuration with the excitation point. The crack is 100 mm from the excitation point and the sensing point, respectively.

As revealed numerically and experimentally [6, 7, 36, 38], the crack-induced second harmonic is lower than a fundamental wave mode by several orders of magnitude. To facilitate extraction of the weak second harmonic from a raw wave signal, the pulse-inversion approach [50, 51] is utilized in simulation, in which the excitation with the same magnitude but in an opposite phase, are applied respectively in two simulated cases, whereby to double the crack-induced second harmonic, and in the meantime cancel the fundamental wave mode – a numerical measure to enhance the extraction and quantification of second harmonics.

Applying the short-time Fourier transform (STFT) [52, 53], **Figs. 12 (a-d)** show the spectra of the fundamental waves and the strengthened second harmonics generated by the crack (of different depths). Using the pulse-inversion approach, the fundamental wave modes are numerically cancelled, leaving the doubled second harmonic modes. As observed, the severer the crack, the more intense the second harmonic generation it will be. On the other hand, the amplitudes of the fundamental waves remain largely unchanged regardless of the change in crack depth, implying that the signal magnitude, a linear characteristic of GUW, is not sensitive to a small-scale crack.

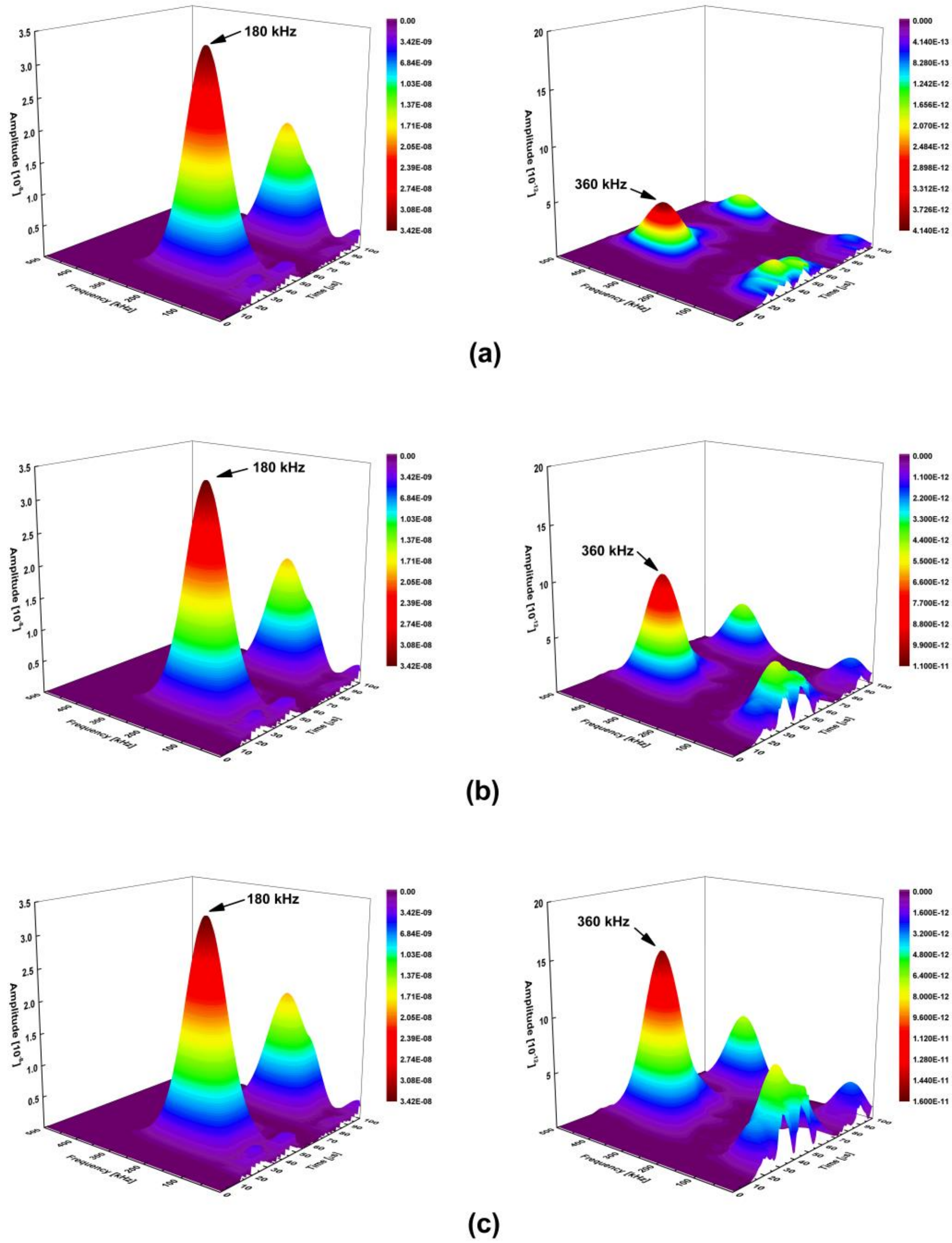

Figure 12. Spectra of the fundamental waves (left) and the enhanced second harmonics (right, in which the fundamental wave modes are numerically cancelled using the pulse-inversion approach [50]) induced by a 'breathing' crack (1mm long), when its depth is (a) 0.5 mm, (b) 1.0 mm, (c) 1.5 mm, and (d) 2.0 mm.

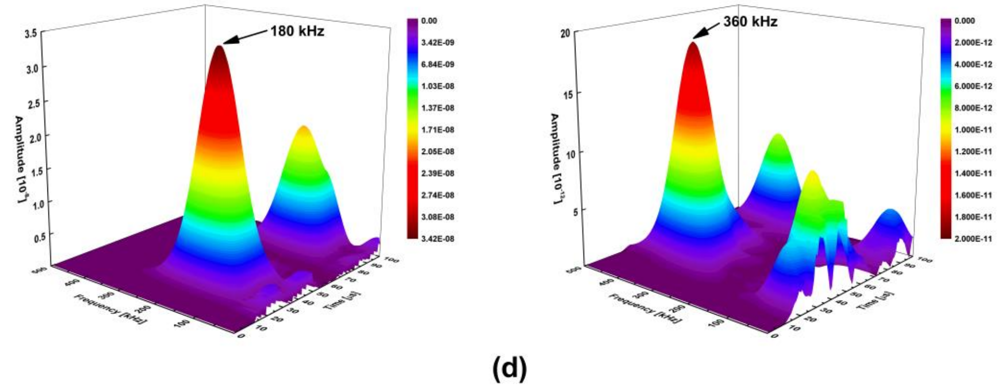

Figure 12. *Cont.*

With the current excitation of 180 kHz, the amplitudes of the second harmonics at the double excitation frequency (360 kHz) are extracted and displayed in **Fig. 13(a)**, clearly suggesting that the magnitudes of the generated second harmonics increase as crack grows. By relating the magnitudes of the second harmonics to the fundamental wave, the nonlinear damage indicator, defined in Eq. (22), can be ascertained.

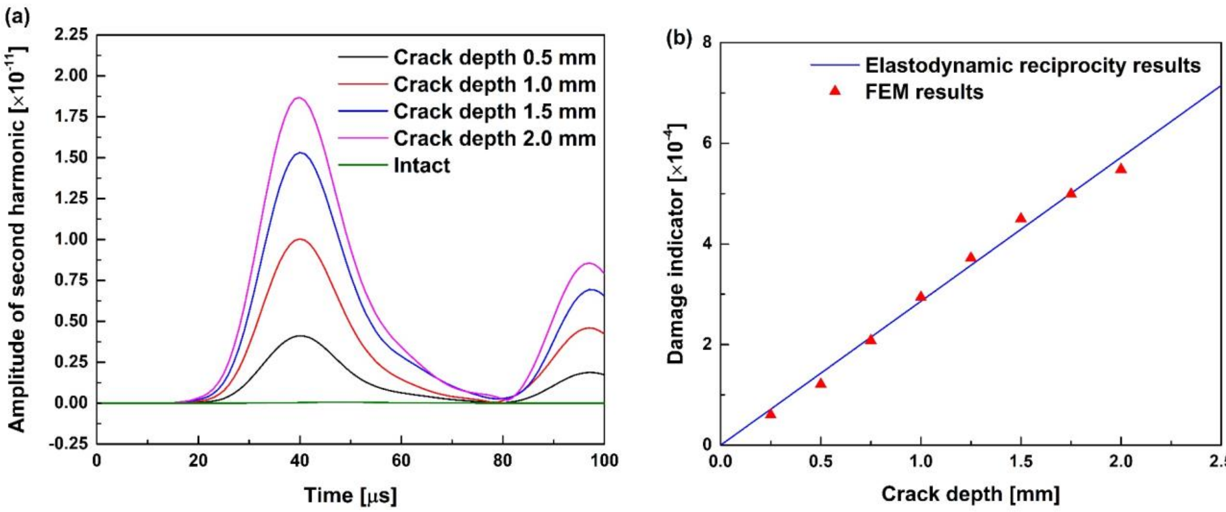

Figure 13. (a) Amplitudes of the generated second harmonic at double excitation frequency; (b) comparison of the nonlinear damage indicator when the crack has different dimensions, obtained from FE simulation and from the analytical model.

Figure 13(b) reveals the nonlinear damage indicator obtained from FE simulation and calculated using Eq. (22), to confirm that the numerical results agree with analytical results. With the magnitude of the fundamental wave using Eq. (15), this analytical model facilitates quantitative estimate of the magnitude of crack-induced second harmonic. In addition, **Fig. 13(b)** argues that the nonlinear indicator is proportional to the crack depth, validating the conclusion drawn in Section 3 that the nonlinear indicator is proportional to the area of the crack surface.

5. Proof-of-concept Validation Using Experiment

Subsequent to FE validation, the analytical model and the closed-form solution are examined experimentally. In experiment, the growth of a non-penetrating corner crack emanating from a fastener hole (a typical embryonic fatigue crack) in its early stage is monitored and calibrated continuously, using the captured second-harmonics in Lamb wave signals.

5.1 Specimen Preparation and Experimental Set-up

Three aluminum (7075-T6) plates (labeled as T1, T2 and T3; each measuring 500 mm long, 80 mm wide and 3 mm thick) are prepared, in each of which a through-thickness fastener hole (diameter: 6 mm) is centralized. The plate is installed on a fatigue testing platform (GP® SDF2000), to perform the fatigue crack growth testing. A triangle notch along the plate thickness is pre-treated (~0.6 mm in both the out-of-plane and in-plane directions) at the fastener hole, in **Fig. 14(a)**, to initiate a non-penetrating fatigue crack under the cyclic fatigue load. A 10 Hz pre-cracking cyclic load with the maximum tensile load of 30 kN and the stress ratio of 0.1 is applied on each sample plate to initiate a corner crack from the tip of the triangle notch. The length and depth of the corner crack are measured using a microscope and a slender mirror inserted into the fastener hole, **Fig. 14(a)**. The pre-cracking process is completed when a quarter-elliptical corner crack of ~1.0 mm in its length and depth from the notch tip, respectively, is reached. Subsequently, the maximum tensile load of the pre-cracking cyclic load is regulated to 20 kN, to perform fatigue crack growth testing. The test is paused after every 1,000 cycles of the fatigue load, and during the interval the length and depth of the corner crack are measured. The nonlinear ultrasonic testing is conducted on an ultrasonic testing system (RITEC®, RAM-5000 SNAP) for determining the magnitudes of the fundamental wave and second harmonics induced by the corner crack. The fatigue crack growth testing is terminated when the fatigue crack penetrates the entire thickness of the plate. Details of the fatigue crack growth testing are summarized in **Tab. 1**.

Table 1. Key observations in fatigue crack growth testing.

Specimen #	Length of the initial fatigue crack (mm)	Depth of the initial fatigue crack (mm)	Cycles to formation of the initial crack	Cycles to formation of a penetrating crack
T1	0.95	0.95	8,000	18,000
T2	0.9	1.0	10,000	23,000
T3	0.85	0.85	6,000	22,000

A lead zirconate titanate (PZT) wafer (PSN-33, diameter: 8 mm; thickness: 0.48 mm), functioning as a wave actuator, is mounted on the surface of each plate, 100 mm from the center of the fastener hole; another PZT wafer, serving as the wave sensor, is mounted 100 mm from the fastener hole, to form a ‘pitch-catch’ configuration, in **Fig. 14(b)**. The excitation – a 5-cycle Hanning-windowed sinusoidal toneburst, is generated by the testing system at a central frequency of 250 kHz, and the crack-triggered wave signals are captured by the sensor using an oscilloscope at the sampling frequency of 200 MHz and averaged for 1,024 times to minimize the measurement uncertainty.

5.2 Results and Discussion

The corner crack progresses continuously in both the length and depth under the cyclic fatigue load, before it develops to a penetrating manner. The length and depth of the corner crack are measured using a microscope and an inserted slender mirror, in **Fig. 15**. It can be observed that in each specimen the corner crack progresses slowly in the pre-cracking stage, behaves a stable growth, and then advances rapidly before it penetrates the thickness of specimen.

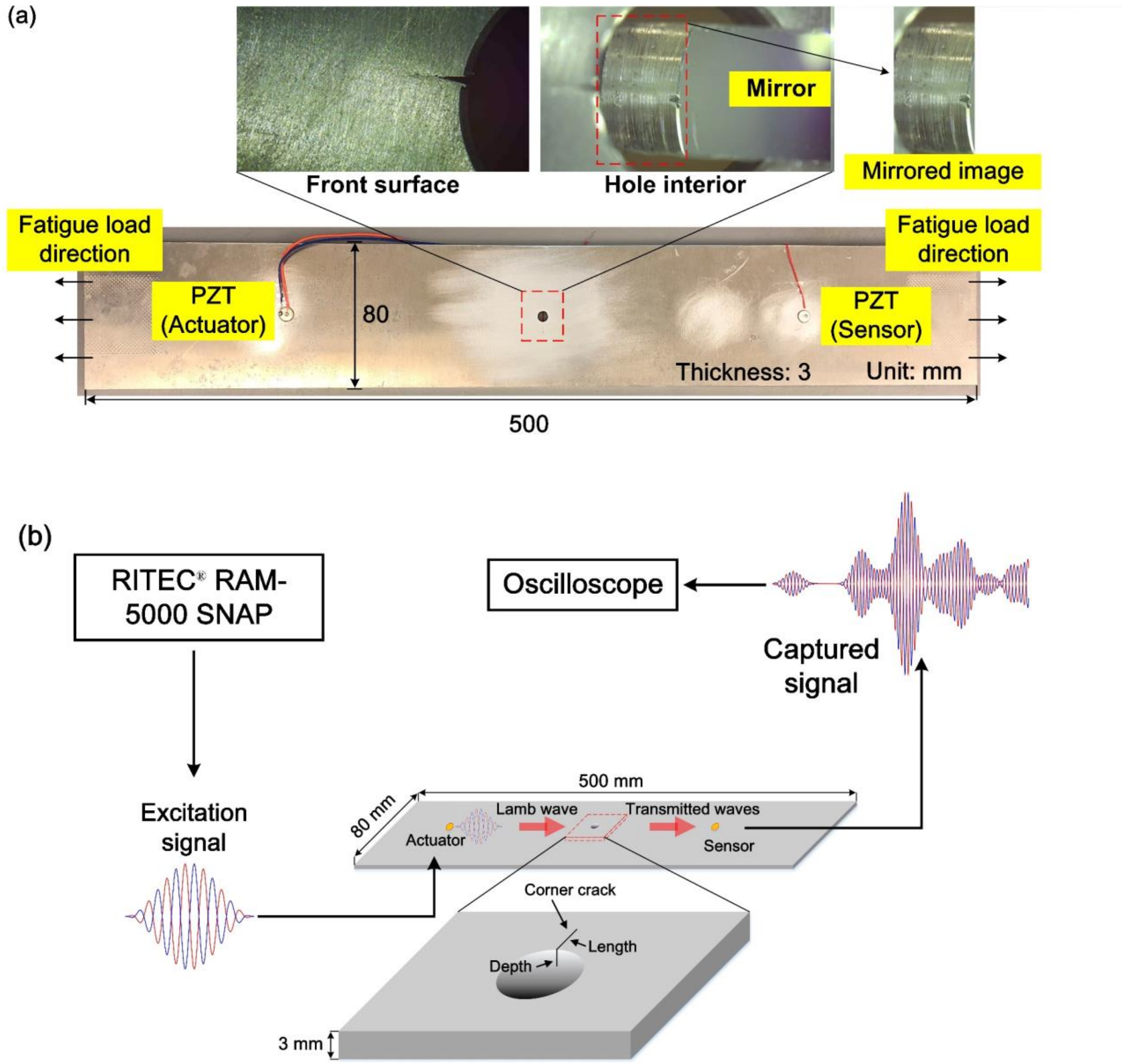

Figure 14. (a) Photographic illustration of the specimen in fatigue testing, and (b) schematic of experimental set-up of nonlinear ultrasonic testing.

The second harmonic induced by the corner crack is extracted from the captured wave signals using the ‘pulse-inversion’ approach during the crack initiation and growth stages. Applied with the STFT-based time-frequency analysis, the amplitudes of both the fundamental wave and the crack-induced second harmonic are obtained, and consequently the nonlinear indicator is calculated using Eq. (22), to calibrate the severity of the crack.

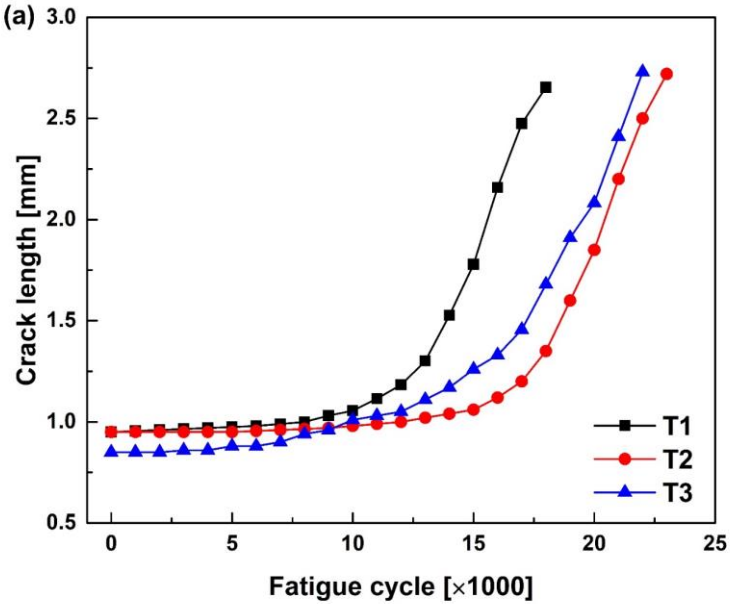

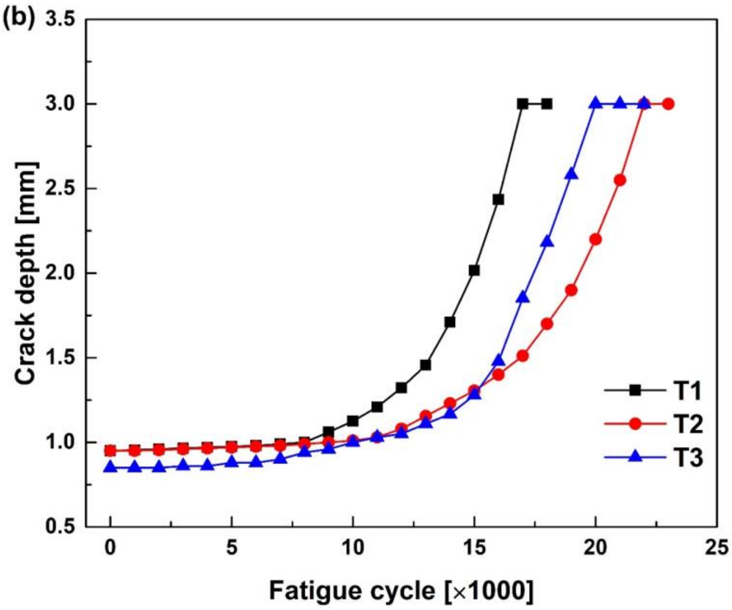

Figure 15. Measured length and depth of the corner crack in specimen (a) T1, (b) T2 and (c) T3.

By way of illustration using specimen T1, **Fig. 16(a)** shows the normalized β as fatigue cycle increases (normalized with regard to its initial value when fatigue testing commences), accentuating three stages which correspond to different stages of the crack growth: crack initiation, stable growth and rapid growth. i) The indicator primarily remains largely unchanged within the first 8,000 fatigue cycles, corresponding to the crack initiation stage during which the crack progresses slowly; ii) from 8,000 to 15,000 fatigue cycles, the indicator increases significantly due to the continuously augmented surface area of the crack during its stable growth stage. In this stage, the corner crack develops steadily in its surface and depth. As a result of the small dimensions, the crack performs the ‘breathing’ behavior when the probing Lamb wave interacts with the crack; iii) beyond the stable growth (>15,000 cycles), the indicator fluctuates within a small range, which corresponds to the rapid growth stage of the crack. The crack deteriorates at a high rate until it penetrates the plate thickness. In this stage, dimensions of the crack are relatively large, and the large crack opening displacement can hardly perform the ‘breathing’ behavior. Therefore, part of the wake region of the crack, especially that near the pre-introduced notch, has ignorable contribution to the second harmonic generation. In another word, although the crack surface area increases rapidly in the last stage, the large crack area contributes insignificant generation of the second harmonic, leading to inapplicability of the nonlinear damage indicator. The same phenomenon is also observed in specimen T2 and T3, as depicted in **Figs. 16(b-c)**.

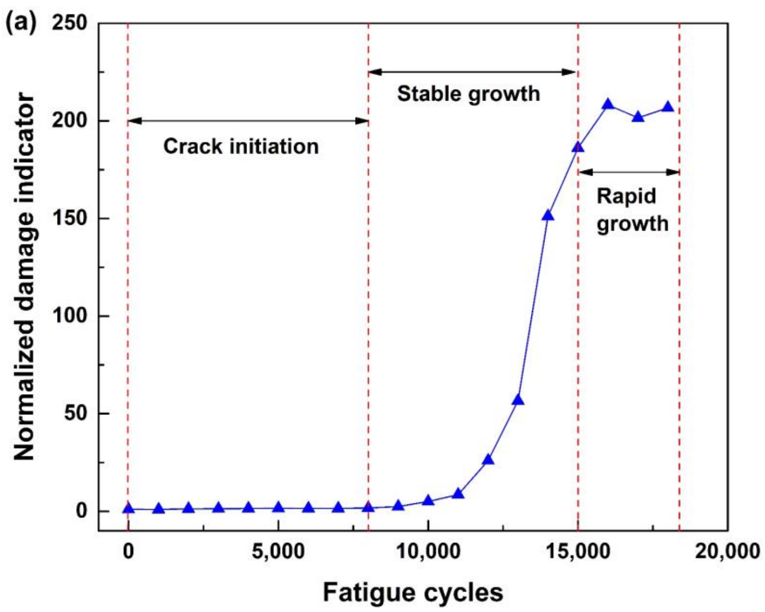

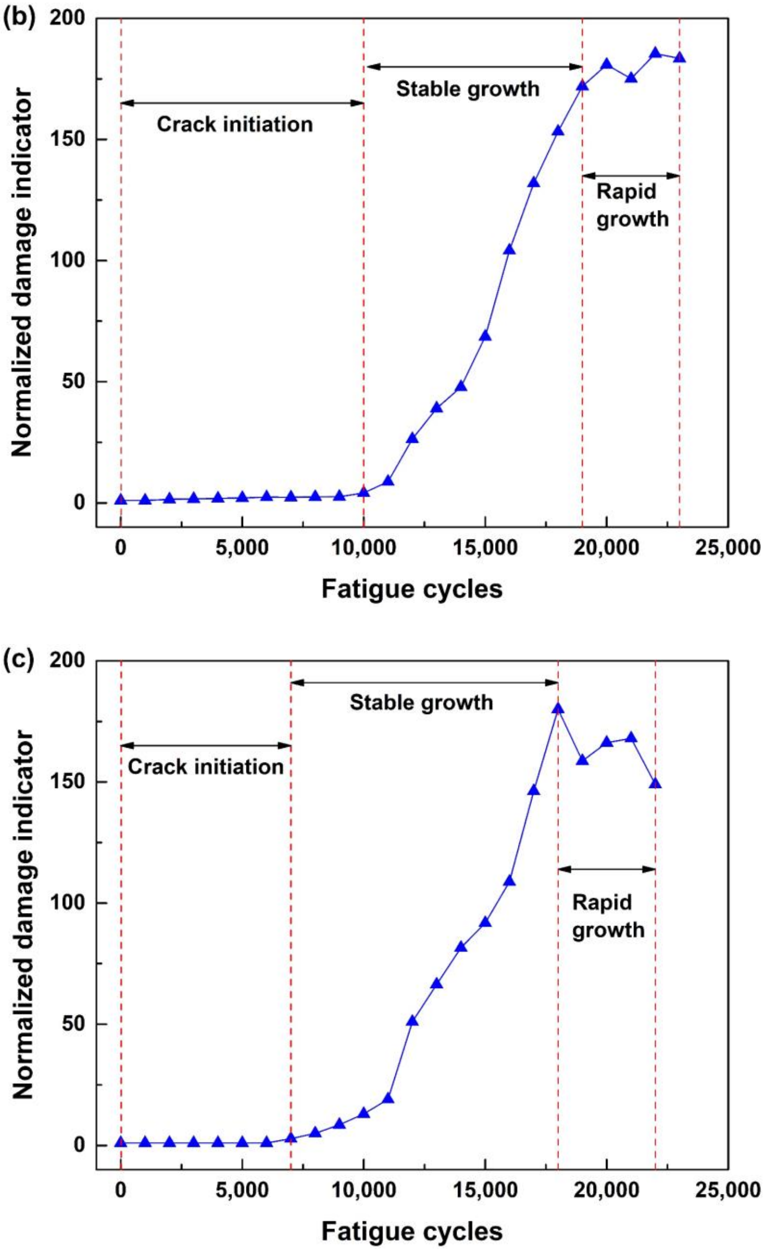

Figure 16. Normalized nonlinear damage indicator against fatigue cycles for specimen (a) T1, (b) T2 and (c) T3.

Figures 17(a-c) present the crack surface area (estimated using measured length and depth) versus normalized β measured during the stable crack growth stage. Here, to eliminate the effect of the irregular crack growth from the triangle notch to the quarter-elliptical fatigue crack during the crack initiation stage, the initial crack surface area is subtracted.

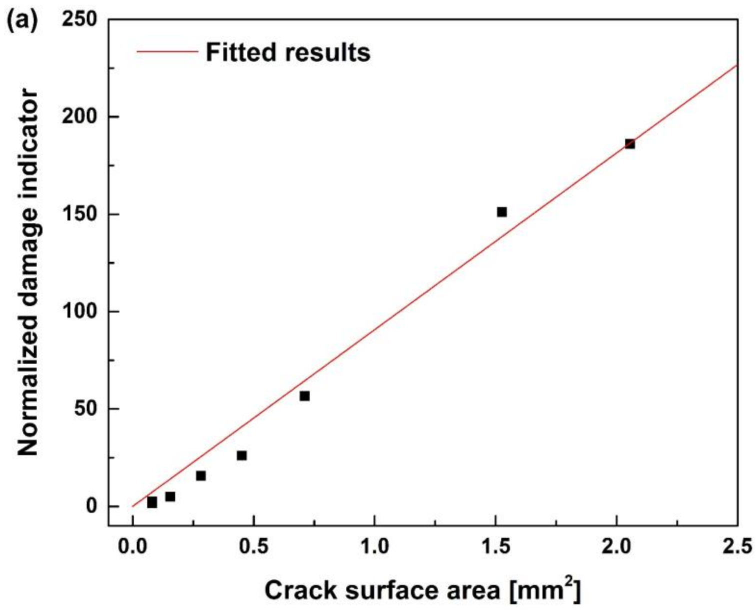

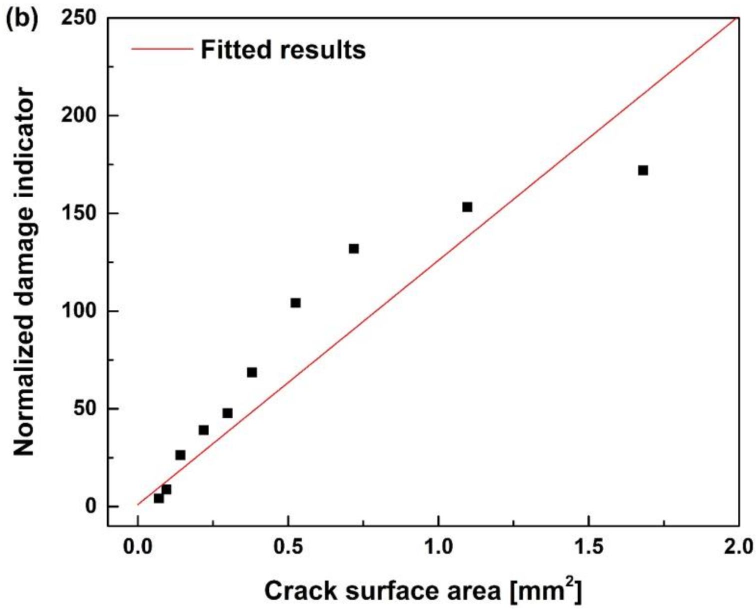

Figure 17. Normalized nonlinear damage indicator against crack surface area during the stable crack growth stage for specimen (a) T1, (b) T2 and (c) T3.

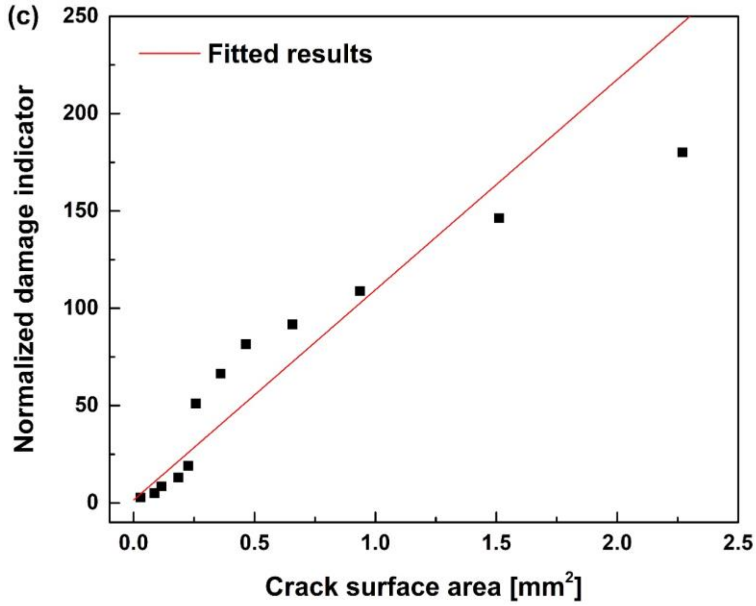

Figure 17. *Cont.*

Figure 17 reveals that the nonlinear indicator increases linearly as the crack surface area expands, validating the conclusion drawn in the theoretical analysis in Section 3 and in FE simulation in Section 4.2 – the magnitude of the second harmonic and the nonlinear indicator are proportional to the crack surface area as a fatigue crack progresses. The deviation of the experimental results from the fitted linear results is mainly caused by i) the bonding condition between the PZT wafers and specimens; and ii) irregular crack initiation from the introduced triangle notch, which leads to error in the measurement of crack surface area. This finding can be beneficial to early awareness and quantitative evaluation of a contact-type defect.

6. Concluding Remarks

In this study, an elastodynamic reciprocity theorem-driven analytical model is developed, aimed at gaining insight into the second harmonic generation by an embryonic fatigue crack with 'breathing' attributes. A second excitation force with time-dependent traits is introduced to supplant the stress at the crack surfaces generated by the probing Lamb wave, to interfere with the original wavefield in the waveguide. By performing the time-frequency analysis, the second excitation force is linked to the generation of the second harmonic in spectra. The magnitudes of the symmetric Lamb wave modes generated by a time-harmonic point force are obtained analytically and explicitly. A closed-form solution to the magnitude of the 'breathing' crack-induced second harmonic is derived, on which basis a nonlinear damage indicator is defined and proven proportional to the crack surface area. The indicator has demonstrated effective in evaluating embryonic fatigue cracks quantitatively. It is noteworthy that the material plasticity-driven increase in the wave nonlinearity is neglectable when compared with that generated by a 'breathing' crack. FE simulation is conducted to verify the analytical model, and the results have demonstrated the validity and accuracy of the model. Experimental results validate the proportional trend of the indicator with respect to crack severity. This new analytical model and the closed-form solution shed light, from the analytical perspective, on the nonlinear interaction between Lamb waves and a small-scale fatigue damage featuring 'breathing' attributes. The developed model facilitates continuous monitoring and quantitative evaluation of an embryonic fatigue crack.

Acknowledgement

The work was supported by a Key Project (No. 51635008) and a General Project (No. 51875492) received from the National Natural Science Foundation of China. Z Su acknowledges the support from the Hong Kong Research Grants Council via General Research Funds (Nos. 15202820, 15204419 and 15212417).

References

[1] K. Wang, M. Liu, Z. Su, S. Guo, F. Cui, Mode-mismatching enhanced disbond detection using material nonlinearity in guided waves at low frequency, Journal of Sound and Vibration, (2020) 115733.

[2] M. Li, M. Deng, G. Gao, Y. Xiang, Modeling of second-harmonic generation of circumferential guided wave propagation in a composite circular tube, Journal of Sound and Vibration, 421 (2018) 234-245.

[3] N. Rauter, R. Lammering, A constitutive model for the analysis of second harmonic Lamb waves in unidirectional composites, International Journal of Solids and Structures, 135 (2018) 184-196.

[4] D. Broda, W. Staszewski, A. Martowicz, T. Uhl, V. Silberschmidt, Modelling of nonlinear crack–wave interactions for damage detection based on ultrasound—A review, Journal of Sound and Vibration, 333 (2014) 1097-1118.

[5] K.H. Matlack, J.-Y. Kim, L.J. Jacobs, J. Qu, Review of second harmonic generation measurement techniques for material state determination in metals, Journal of Nondestructive Evaluation, 34 (2015) 273.

[6] Y. Yang, C.-T. Ng, A. Kotousov, H. Sohn, H.J. Lim, Second harmonic generation at fatigue cracks by low-frequency Lamb waves: Experimental and numerical studies, Mechanical Systems and Signal Processing, 99 (2018) 760-773.

[7] K. Wang, Y. Li, Z. Su, R. Guan, Y. Lu, S. Yuan, Nonlinear aspects of "breathing" crack-disturbed plate waves: 3-D analytical modeling with experimental validation, International Journal of Mechanical Sciences, 159 (2019) 140-150.

[8] L. Xu, K. Wang, X. Yang, Y. Su, J. Yang, Y. Liao, P. Zhou, Z. Su, Model-driven fatigue crack characterization and growth prediction: A two-step, 3-D fatigue damage modeling framework for structural health monitoring, International Journal of Mechanical Sciences, 195 (2021) 106226.

[9] H. Chen, G. Zhang, D. Fan, L. Fang, L. Huang, Nonlinear Lamb Wave Analysis for Microdefect Identification in Mechanical Structural Health Assessment, Measurement, (2020) 108026.

[10] K. Wang, M. Liu, Z. Su, S. Yuan, Z. Fan, Analytical insight into “breathing” crack-induced acoustic nonlinearity with an application to quantitative evaluation of contact cracks, Ultrasonics, 88 (2018) 157-167.

[11] Z. Su, C. Zhou, M. Hong, L. Cheng, Q. Wang, X. Qing, Acousto-ultrasonics-based fatigue damage characterization: Linear versus nonlinear signal features, Mechanical Systems and Signal Processing, 45 (2014) 225-239.

[12] W. Cao, K. Wang, P. Zhou, X. Yang, L. Xu, M. Liu, P. Fromme, B. Pang, R. Chi, Z. Su, Nonlinear ultrasonic evaluation of disorderedly clustered pitting damage using an in situ sensor network, Structural Health Monitoring, 19 (2020) 1989-2006.

[13] A. Spada, M. Capriotti, F.L. di Scalea, Global-Local model for guided wave scattering problems with application to defect characterization in built-up composite structures, International Journal of Solids and Structures, 182 (2020) 267-280.

[14] Y. Lu, L. Ye, Z. Su, C. Yang, Quantitative assessment of through-thickness crack size based on Lamb wave scattering in aluminium plates, NDT & e International, 41 (2008) 59-68.

[15] M. Lowe, O. Diligent, Low-frequency reflection characteristics of the s 0 Lamb wave from a rectangular notch in a plate, The Journal of the Acoustical Society of America, 111 (2002) 64-74.

[16] N. Mori, S. Biwa, T. Hayashi, Reflection and transmission of Lamb waves at an imperfect joint of plates, Journal of Applied Physics, 113 (2013) 074901.

[17] L. Qiu, S. Yuan, F.-K. Chang, Q. Bao, H. Mei, On-line updating Gaussian mixture model for aircraft wing spar damage evaluation under time-varying boundary condition, Smart materials and structures, 23 (2014) 125001.

[18] J. Chen, S. Yuan, X. Jin, On-line prognosis of fatigue cracking via a regularized particle filter and guided wave monitoring, Mechanical Systems and Signal Processing, 131 (2019) 1-17.

[19] S. Yuan, J. Chen, W. Yang, L. Qiu, On-line crack prognosis in attachment lug using Lamb wave-deterministic resampling particle filter-based method, Smart Materials and Structures, 26 (2017) 085016.

[20] K. Wang, W. Cao, L. Xu, X. Yang, Z. Su, X. Zhang, L. Chen, Diffuse ultrasonic wave-based structural health monitoring for railway turnouts, Ultrasonics, 101 (2020) 106031.

[21] K. Xu, D. Ta, Z. Su, W. Wang, Transmission analysis of ultrasonic Lamb mode conversion in a plate with partial-thickness notch, Ultrasonics, 54 (2014) 395-401.

[22] J.H. Cantrell, W.T. Yost, Acoustic nonlinearity and cumulative plastic shear strain in cyclically loaded metals, Journal of Applied Physics, 113 (2013) 153506.

[23] M. Liu, G. Tang, L.J. Jacobs, J. Qu, Measuring acoustic nonlinearity parameter using collinear wave mixing, Journal of applied physics, 112 (2012) 024908.

[24] C. Yeung, C.T. Ng, Nonlinear guided wave mixing in pipes for detection of material nonlinearity, Journal of Sound and Vibration, 485 (2020) 115541.

[25] I.Y. Solodov, N. Krohn, G. Busse, CAN: an example of nonclassical acoustic nonlinearity in solids, Ultrasonics, 40 (2002) 621-625.

[26] S. Biwa, S. Nakajima, N. Ohno, On the acoustic nonlinearity of solid-solid contact with pressure-dependent interface stiffness, J. Appl. Mech., 71 (2004) 508-515.

[27] A. Hikata, B.B. Chick, C. Elbaum, Dislocation contribution to the second harmonic generation of ultrasonic waves, Journal of Applied Physics, 36 (1965) 229-236.

[28] A. Hikata, C. Elbaum, Generation of ultrasonic second and third harmonics due to dislocations. I, Physical Review, 144 (1966) 469.

[29] W. Cash, W. Cai, Dislocation contribution to acoustic nonlinearity: The effect of orientation-dependent line energy, Journal of applied Physics, 109 (2011) 014915.

[30] Z. Chen, J. Qu, Dislocation-induced acoustic nonlinearity parameter in crystalline solids, Journal of Applied Physics, 114 (2013) 164906.

[31] J.H. Cantrell, W.T. Yost, Nonlinear ultrasonic characterization of fatigue microstructures, International Journal of fatigue, 23 (2001) 487-490.

[32] T. Apple, J. Cantrell, C. Amaro, C. Mayer, W. Yost, S. Agnew, J. Howe, Acoustic harmonic generation from fatigue-generated dislocation substructures in copper single crystals, Philosophical Magazine, 93 (2013) 2802-2825.

[33] L.F. Rose, B.S. Vien, W.K. Chiu, Analytical solutions for crack-like scatterers and sources in isotropic elastic plates, Wave Motion, 93 (2020) 102476.

[34] C. Yang, J.D. Achenbach, Time domain scattering of elastic waves by a cavity, represented by radiation from equivalent body forces, International Journal of Engineering Science, 115 (2017) 43-50.

[35] C. Wang, O. Balogun, J.D. Achenbach, Scattering of a Rayleigh wave by a near surface crack which is normal to the free surface, International Journal of Engineering Science, 145 (2019) 103162.

[36] Y. Shen, V. Giurgiutiu, Predictive modeling of nonlinear wave propagation for structural health monitoring with piezoelectric wafer active sensors, Journal of Intelligent Material Systems and Structures, 25 (2014) 506-520.

[37] Y. Yang, C.-T. Ng, A. Kotousov, Influence of crack opening and incident wave angle on second harmonic generation of Lamb waves, Smart Materials and Structures, 27 (2018) 055013.

[38] Y. Zhao, F. Li, P. Cao, Y. Liu, J. Zhang, S. Fu, J. Zhang, N. Hu, Generation mechanism of nonlinear ultrasonic Lamb waves in thin plates with randomly distributed micro-cracks, Ultrasonics, 79 (2017) 60-67.

[39] X. Ding, Y. Zhao, M. Deng, G. Shui, N. Hu, One-way Lamb mixing method in thin plates with randomly distributed micro-cracks, International Journal of Mechanical Sciences, 171 (2020) 105371.

[40] V.E. Nazarov, A.M. Sutin, Nonlinear elastic constants of solids with cracks, The Journal of the Acoustical Society of America, 102 (1997) 3349-3354.

[41] J.H. Cantrell, Ultrasonic harmonic generation from fatigue-induced dislocation substructures in planar slip metals and assessment of remaining fatigue life, Journal of Applied Physics, 106 (2009) 093516.

[42] Achenbach, D. Jan, Reciprocity and Related Topics in Elastodynamics, Applied Mechanics Reviews, 59 (2006) 13-32.

[43] J. Achenbach, Acoustic emission from a surface-breaking crack in a layer under cyclic loading, Journal of Mechanics of Materials and Structures, 4 (2009) 649-657.

[44] B. Dubuc, S. Livadiotis, A. Ebrahimkhanlou, S. Salamone, Crack-induced guided wave motion and modal excitability in plates using elastodynamic reciprocity, Journal of Sound and Vibration, 476 (2020) 115287.

[45] O. Buck, W. Morris, J.M. Richardson, Acoustic harmonic generation at unbonded interfaces and fatigue cracks, Applied Physics Letters, 33 (1978) 371-373.

[46] K. Dziedziech, L. Pieczonka, P. Kijanka, W.J. Staszewski, Enhanced nonlinear crack-wave interactions for structural damage detection based on guided ultrasonic waves, Structural control and health monitoring, 23 (2016) 1108-1120.

[47] I.Y. Solodov, Ultrasonics of non-linear contacts: propagation, reflection and NDE-applications, Ultrasonics, 36 (1998) 383-390.

[48] J.D. Achenbach, Y. Xu, Wave motion in an isotropic elastic layer generated by a time-harmonic point load of arbitrary direction, Journal of the Acoustical Society of America, 106 (1999) 83-90.

[49] J.D. Achenbach, Calculation of wave fields using elastodynamic reciprocity, International Journal of Solids & Structures, 37 (2000) 7043-7053.

[50] Y. Ohara, K. Kawashima, R. Yamada, H. Horio, Evaluation of amorphous diffusion bonding by nonlinear ultrasonic method, in: AIP Conference Proceedings, American Institute of Physics, 2004, pp. 944-951.

[51] J.-Y. Kim, L.J. Jacobs, J. Qu, J.W. Littles, Experimental characterization of fatigue damage in a nickel-base superalloy using nonlinear ultrasonic waves, The Journal of the Acoustical Society of America, 120 (2006) 1266-1273.

[52] S. Mallat, A wavelet tour of signal processing, Elsevier, 1999.

[53] S. Nagarajaiah, N. Varadarajan, Short time Fourier transform algorithm for wind response control of buildings with variable stiffness TMD, Engineering Structures, 27 (2005) 431-441.